Driving viscous hydrodynamics in bulk electron flow in graphene using micromagnets

Jack N. Engdahl,[1,*] Aydın Cem Keser,[2] Thomas Schmidt,[3,4] and Oleg P. Sushkov[1]
[1]*School of Physics, University of New South Wales, Sydney 2052, Australia*
[2]*CSIRO, Bradfield Road, West Lindfield NSW 2070, Australia*
[3]*Department of Physics and Materials Science, University of Luxembourg, Luxembourg*
[4]*School of Chemical and Physical Sciences, Victoria University of Wellington, P.O. Box 600, Wellington 6140, New Zealand*

(Received 14 December 2023; revised 9 April 2024; accepted 11 April 2024; published 2 May 2024)

We consider the hydrodynamic flow of an electron fluid in a channel formed in a two-dimensional electron gas (2DEG) with no-slip boundary conditions. To generate vorticity in the fluid, the flow is influenced by an array of micromagnets on the top of the 2DEG. We analyze the viscous boundary layer, and we demonstrate anti-Poiseuille behavior in this region. Furthermore, we predict a longitudinal voltage modulation, where a periodic magnetic field generates a voltage term periodic in the direction of transport. From an experimental point of view, we propose a method for a boundary-independent measurement of the viscosity of different electron fluids. The results are applicable to graphene away from the charge-neutrality point and to semiconductors.

DOI: 10.1103/PhysRevB.109.195402

I. INTRODUCTION

It has been over half a century since the theory of viscous electron hydrodynamics was first developed [1], and in recent years viscous effects have been observed in the electron fluid experimentally [2,3]. Electron transport transitions to the hydrodynamic regime when the momentum-conserving electron-electron scattering length, l_{ee}, is the shortest length scale in the system, and it becomes much shorter than the momentum-nonconserving diffusive scattering length, l_{mfp}, and the width of the sample, W. In this regime, electron-electron interactions dominate and a local thermodynamic equilibrium is established among the electrons, enabling them to flow as a fluid. Since this condition requires samples of very high purity, the theoretical prediction of the hydrodynamic regime in the 1960s [1,4] could only be realized experimentally after the development of high-mobility semiconductors [5] and graphene [2,6].

Hydrodynamic electron flow manifests itself in a range of effects that have been observed. While hydrodynamic electron transport was suggested to have been achieved already in 1995 in Ref. [5], this result was immediately challenged by Gurzhi in Ref. [7]: the conditions for hydrodynamics in the bulk material were satisfied, but they were not satisfied for hydrodynamics in a 2DEG. It was not until 2016 that reliable evidence of hydrodynamic transport was presented in Refs. [8–10]. Signatures of hydrodynamic behavior include the decrease of resistance with increasing temperature, called the Gurzhi effect [5,11–15], large negative magnetoresistance[1] [10,13,17–21], Poiseuille flow profiles [22–24], Hall viscosity [14,25], negative nonlocal resistance and the formation of whirlpools [8,26–28], the development of local viscous regions [29], the violation of the Wiedemann-Franz law[2] [31–35], resonant photoresistance in magnetic fields [20,36–39], anomalous scaling of the resistance with the channel width [9,32], and a quantum-critical dynamic conductivity [40]. Moreover, novel phenomena have been predicted, such as anisotropic fluids [41,42], the elimination of the Landauer-Sharvin resistance [43], the dynamo effect in the electron-hole plasma [44], and the possibility of hydrodynamic spin transport [45–47] inspired by experiments on liquid mercury [48,49]. In addition to the Poiseuille-like flow expected from electron hydrodynamics, anomalous flow profiles have been predicted in the boundary layer in charge neutral graphene in a uniform perpendicular magnetic field, with this "anti-Poiseuille" flow attributed to recombination effects [50–52].

Hydrodynamic flow depends qualitatively on boundary conditions, with no-slip boundaries giving rise to the well-known Poiseuille flow profile. On the other hand, it is also possible to achieve perfect-slip boundaries by using gates to create a channel in a clean semiconductor. This unique property was used in Ref. [13] for precise measurements of the viscosity in clean GaAs. The measurements indicate deviations from the predictions of the conventional theory of electron-electron scattering, and this exciting observation requires more careful studies.

There exists a generic problem in electron hydrodynamics, namely disentangling Ohmic effects, boundary effects, and hydrodynamic effects in experimental data. Viscous dissipation is proportional to the vorticity of the fluid, while the Ohmic dissipation is independent of vorticity. To enhance hydrodynamics, one thus needs to enhance the vorticity. This might be achieved by generating turbulent flow of the electron fluid, but the electron fluid is extraordinarily vis-

*j.engdahl@student.unsw.edu.au

[1]The viscous origin of negative magnetoresistance in high-purity samples is disputed [16], therefore the magnetic field dependence of viscosity is an open question.

[2]Although recent work in Ref. [30] suggests that the result of a well-known experimental work [31] is not hydrodynamic in nature.

cous and therefore it is practically impossible to approach turbulence.

In the laminar regime in a uniform magnetic field, vorticity is generated only near the boundaries of the channel in a layer of width $\sim\sqrt{l_{\rm ee}l_{\rm mfp}}$. The flow in this boundary layer is influenced not only by the viscous fluid effects, but also by the boundary conditions that are device-specific and typically not well known. Therefore, it is hard to disentangle the unknown boundary effects and unknown viscous effects.

In Ref. [13] the problem was partially resolved by using a gated channel in a GaAs 2DEG that supports perfect-slip boundary conditions. This allowed for relatively accurate measurements of the viscosity of the electron fluid. However, the accuracy of the measurements was limited by Ohmic dissipation, which was more than an order of magnitude larger than the viscous one.

In Ref. [53] we suggested a method that involved the use of micromagnets to create wiggling hydrodynamic flow and hence create vorticity throughout the bulk of the sample, not just in the boundary region. This allows for a dramatic enhancement of viscous hydrodynamic dissipation. Hydrodynamics in a finite channel is inherently a boundary problem, and in Ref. [53] the problem was solved only for a straight channel in the unique case of perfect-slip boundaries. In the present work, we extend the method to a straight channel with arbitrary boundary conditions, either no-slip or finite-slip boundaries. Of course the bulk solution is the same, but the structure of the viscous boundary layer depends on the boundary condition, and we determine the structure in the present work. Hence, the present work extends the magneto-hydrodynamic method to graphene and also to δ-doped semiconductors. The results of this work allow for the viscosity of the electron fluid to be extracted from a measurement of longitudinal resistivity of a finite straight channel in such devices.

The structure of this paper is as follows. In Sec. II we describe the solution for the bulk flow through a sinusoidal magnetic field found in Ref. [53]. The difference from Ref. [53] is that we present numerical estimates for graphene instead of GaAs. In Sec. III we study the boundary layer in a straight channel using the no-slip boundary condition, and we characterize the flow near the boundary. We first solve the boundary conditions using perturbation theory, and then we expand this idea to develop a numerically exact solution. The key results of Sec. III are the width of the boundary layer and the emergence of pseudo anti-Poiseuille flow at high magnetic field strengths. Understanding the width of the boundary layer allows a lower limit to be placed on the sample size in order to use the bulk solution for the "zigzag" flow. In Sec. IV we present numerical solution of the model developed in Sec. III and show plots of dissipation and velocity profile. Of theoretical interest, we predict anomalous velocity profiles at high magnetic field that show anti-Poiseuille flow behaviour. In Sec. V we complement our previous numerical solution with a conventional finite element model and qualtitatively reproduce the flow profile. In Sec. VI we calculate the magnetic field of periodic ferromagnetic stripes and hence determine parameters of micromagnets necessary for the experimental setup assuming monolayer graphene with experimentally realistic density and mobility. Section VII presents our conclusions.

II. BULK SOLUTION FOR ELECTRON HYDRODYNAMICS IN A SINUSOIDAL MAGNETIC FIELD

We consider a channel that is sufficiently wide such that boundary layers are much thinner than the channel width, allowing for the bulk flow to be analyzed independently of the boundary conditions. In this regime, the fluid motion of the bulk may be analyzed in the limit of an infinitely wide channel.

Consider a two-dimensional channel where x is the longitudinal direction, y is the transverse direction, and z is perpendicular to the plane. The electron fluid may be controlled through the Lorentz force and thus obeys the stationary Navier-Stokes equation at constant density [54],

$$\frac{\mathbf{v}}{\tau}-\nu\nabla^2\mathbf{v}+\mathbf{v}\cdot\nabla\mathbf{v}=-\frac{\nabla\Phi}{m^*}+\frac{q}{m^*}\mathbf{v}\times\mathbf{B},$$
$$\nabla\cdot\mathbf{v}=\mathbf{0}. \tag{1}$$

Here, $\mathbf{v}$ is the fluid velocity field, τ is the relaxation time related to momentum-nonconserving scattering from impurities and phonons, ν is the kinematic viscosity, Φ is the electrochemical potential, m^* is the effective hydrodynamic mass, q is the fluid particle charge, and $\mathbf{B}$ is the magnetic field. For a uniform field, it is known that this equation predicts the usual Hall effect, whereas recently it has been realized that nonuniform fields have remarkable consequences such as a local suppression of flow [55] and vortex layers in the bulk [53]. The electron-electron scattering length, $l_{\rm ee}$, and the momentum diffusive scattering length, $l_{\rm mfp}$, are defined by the following relations:

$$\nu=\frac{l_{\rm ee}v_F}{4},\quad \tau=\frac{l_{\rm mfp}}{v_F}, \tag{2}$$

where v_F is the Fermi velocity at zero temperature.

The Navier-Stokes Eq. (1) is valid in the limit when $l_{\rm ee}$ is much smaller than all geometric scales in the problem. There are two kinds of subleading corrections to the Navier-Stokes equation [10,56]. The correction of the first kind, the dependence of viscosity on magnetic field, is parametrically proportional to $(l_{\rm ee}/r_c)^2$, where $r_c=mv_F/(eB)$ is the cyclotron radius, and the correction of the second kind, the Hall viscosity, is parametrically proportional to $(l_{\rm ee}/a)^2$, where a is the characteristic geometric scale. We start from the correction of the second kind, which leads to the following modification of the Navier-Stokes equation:

$$\frac{\mathbf{v}}{\tau}-\nu\nabla^2\mathbf{v}+\mathbf{v}\cdot\nabla\mathbf{v}=\left(1+\frac{l_{\rm ee}^2}{2}\nabla^2\right)\mathbf{F},$$
$$\mathbf{F}=-\frac{\nabla\Phi}{m^*}+\frac{q}{m^*}\mathbf{v}\times\mathbf{B}. \tag{3}$$

The term $(l_{\rm ee}^2/2)\nabla^2$ acting on the Lorentz force, $(q/m^*)\mathbf{v}\times\mathbf{B}$, is literally the "Hall viscosity" term from Ref. [10]. The term $(l_{\rm ee}^2/2)\nabla^2$ acting on the gradient of electrochemical potential, $-\nabla\Phi/m^*$, can be easily derived using the method used in Ref. [10]. The electrochemical potential is a sum of the electrostatic part and the pressure part, $\Phi=\Phi_E+\Phi_{\rm pr}$. Strictly speaking, the $(l_{\rm ee}^2/2)\nabla^2$ correction acts only on the electrostatic part. Since $\Phi_E\gg\Phi_{\rm pr}$, we disregard this very small difference. Note that the term $(l_{\rm ee}^2/2)\nabla^2\mathbf{F}$ is time-even, unlike the dissipative viscosity term $\nu\nabla^2\mathbf{v}$, which is time-odd. As

this modified equation is the Navier-Stokes plus the leading correction towards the kinetic equation, we call Eq. (3) the NS^+ equation.

A superlattice of micromagnets modulated in the x direction generates a sinusoidal magnetic field along the z direction in the plane of the 2DEG,

$$B_z = B_0 \sin(gx), \tag{4}$$

where $g = 2\pi/a$, and a is the separation between adjacent micromagnets. As previously mentioned, the electron fluid is very viscous, so the "Bernoulli term," $\mathbf{v}\cdot\nabla\mathbf{v}$, on the left-hand side of Eq. (3) can be neglected. This is because compared to the diffusion term $-\nu\nabla^2\mathbf{v}$, the Bernoulli term scales with the Reynolds number $\mathrm{Re} = vL/\nu$, where L is a characteristic length of the system. In this case, the characteristic length scale is defined by the gradient operator, so an appropriate estimate is $L \approx 3D$, and upon substituting in appropriate parameters later defined in Eq. (11), we see $\mathrm{Re} \approx 10^{-3}$. Hence, we obtain a linear NS^+ equation that can be solved using the stream function ψ defined by $v_x = \partial_y\psi$ and $v_y = -\partial_x\psi$. For an infinitely long and infinitely wide channel with fixed averaged current density $\mathbf{J} = qnv_0\hat{\mathbf{x}}$, the solution is

$$\psi_\infty = v_0\left(y + \frac{C\omega\tau}{g(1+D^2g^2)}\cos(gx)\right),$$
$$C = 1 - g^2 l_{ee}^2/2 \tag{5}$$

where $D = \sqrt{\nu\tau} = \frac{1}{2}\sqrt{l_{ee}l_{mfp}}$ is the characteristic viscous length, and $\omega = |e|B_0/m^*$ is the cyclotron frequency. The viscous and Ohmic dissipation rates follow directly from Eq. (5), where L and W are the length and the width of the channel, respectively,

$$\dot{E}_\Omega = \frac{nm^*}{\tau}\int d^2r\, v^2,$$
$$\dot{E}_\nu = -nm^*\nu\int d^2r\, \mathbf{v}\cdot\nabla^2\mathbf{v}. \tag{6}$$

Note that generally for the incompressible Navier-Stokes equation, the expression for viscous dissipation may be explicitly split up into a bulk stress term and a boundary stress term [54], however for a periodic driving force the boundary term vanishes over an integer number of periods and vanishes when the flow at the inlet and outlet becomes uniform. The boundary stress term is also negligible when the channel length $L \to \infty$. We consider the long channel limit here, but it is also simple to ensure the other two cases are met via design of the device. For the bulk solution (5), Eqs. (6) give

$$\dot{E}_\Omega = \frac{nm^*v_0^2}{\tau}\left(1 + \frac{C^2\omega^2\tau^2}{2(1+D^2g^2)^2}\right)LW,$$
$$\dot{E}_\nu = \frac{nm^*v_0^2}{\tau}\,\frac{C^2g^2D^2\omega^2\tau^2}{2(1+D^2g^2)^2}LW. \tag{7}$$

These equations differ from a similar solution in Ref. [53] by account of the leading gradient expansion correction, $C = 1 \to C = 1 - g^2l_{ee}^2/2$. Equation (7) determine longitudinal resistance of a long and sufficiently wide channel. If the channel has about 50 micromagnets along the length, then the dissipation in the contacts is negligible compared to the bulk dissipation (not more than 1–2 %), and such a channel is said to be sufficiently long. The sufficient width is a more delicate issue, and this question is addressed in Sec. III, where we discuss the solution for the boundary layer. Hence we propose to measure the longitudinal resistance of a sufficiently long and sufficiently wide conducting channel. The diffusive mean free time τ can be determined from the measurement at zero magnetic field. Further measurements of the dependence of the resistance on the amplitude of the magnetic field allows the extraction of l_{ee} and hence allows one to determine the viscosity ν. Explicitly, this is achieved by taking the ratio of the total resistivity and the Drude resistivity,

$$\frac{\rho_{\mathrm{Tot}}}{\rho_D} = \frac{\dot{E}_\Omega + \dot{E}_\nu}{\dot{E}_\Omega(\omega=0)} = 1 + \frac{C^2\omega^2\tau^2}{2(1+D^2g^2)}. \tag{8}$$

So far we have not explicitly solved for the electrochemical potential in the Stokes equation (1). Substituting $\mathbf{v}$ calculated from the stream function (5), it is easy to derive an expression for the electrochemical potential, representing the external force on each fluid particle,

$$\partial_x\Phi = -\frac{m^*v_0}{\tau}\left(1 + \frac{C^2\omega^2\tau^2\sin^2(gx)}{1+D^2g^2}\right),$$
$$\partial_y\Phi = 0. \tag{9}$$

The electrochemical potential does not vary in y in an infinite sample as there is translational symmetry in the y direction, whereas the periodic structure of the magnetic field in the x direction gives rise to a modulated electrochemical potential as a function of x. Furthermore, it is clear that the rate of work done by the external force $\dot{E} = -\int d^2r\, \mathbf{v}\cdot\nabla\Phi$ matches the total dissipation $\dot{E}_\Omega + \dot{E}_\nu$ obtained in Eq. (7).

As the electron number density is approximately constant throughout the sample,[3] the thermodynamic pressure gradients vanish. Therefore, the electrochemical potential gradients are predominantly electric in nature, and we can write the voltage as $\varphi = -\Phi/|e|$,

$$\varphi = \frac{m^*v_0}{|e|\tau}\left[x + \frac{C^2\omega^2\tau^2}{2(1+D^2g^2)}\left(x - \frac{\sin(2gx)}{2g}\right)\right]. \tag{10}$$

From Eq. (10) it is clear that the electric field varies with x. As this effect arises from the presence of a periodic magnetic field and the modulation in voltage is in the same direction as transport, it is appropriate to label this a "magnetic field driven longitudinal voltage modulation."

Electron transport in high-mobility graphene may be hydrodynamic in the temperature range $150 \leqslant T < 300$ K [3]. To be specific, we will present numerical estimates for a monolayer graphene device with mobility $\mu \approx 2\times 10^5$ cm^2/Vs and density $n \approx 10^{12}$ cm^{-2} at a temperature $T = 220$ K with parameters similar to the device used in Ref. [8],

$$n = 10^{12}\ \mathrm{cm}^{-2}, \quad T = 220\ \mathrm{K}, \quad l_{\mathrm{mfp}} = 1.9\ \mu\mathrm{m},$$
$$l_{ee} = 0.24\ \mu\mathrm{m}, \quad \tau = 1.9\ \mathrm{ps}. \tag{11}$$

For a magnetic field amplitude $B_0 = 75$ mT this gives $\omega\tau = 1.2$. Here we keep in mind that the hydrodynamic mass for monolayer graphene is $m^* = p_F/v_F$, with Fermi momentum $p_F = \hbar\sqrt{n\pi}$, accounting for spin and valley degeneracy in

[3] See the discussion leading to and following Eq. (12).

graphene. With these parameters the characteristic viscous length is $D \approx 0.34$ μm.

Ohmic dissipation (7) is dependent on the dimensionless parameters $\omega\tau$ and gD, which, for fixed $\omega\tau$, may be shown to be maximized at $gD = [1 + (C\omega\tau)^2/2]^{1/4}$. We take $g = 2.6\,\mu\text{m}^{-1}$, which is slightly smaller than the optimal value and which corresponds to lattice spacing $a = 2.5$ μm. At a larger value of g (smaller a), the gradient non-Stokes correction $l_{ee}^2\nabla^2/2 \to l_{ee}^2 g^2/2$ is too large. At $a = 2.5$ μm the correction is $l_{ee}^2 g^2/2 = 0.19$.

With these parameters and assuming $v_0 = 100$ m/s, corresponding to $I = 0.15$ μA per μm of channel width from Ref. [8], the oscillation amplitude of the longitudinal voltage modulation is approximately 0.3 μV. Of course the amplitude can be increased by increasing the current.

So far in the analysis we have assumed the electron fluid is incompressible as the number density is made approximately constant via a gate voltage. To check the validity of this assumption, let us compare the gate voltage φ_g that determines the electron density with the longitudinal voltage drop φ,

$$\varphi_g \approx \frac{ned}{\epsilon}, \quad \varphi \sim \frac{m^* v_0}{|e|\tau} L. \tag{12}$$

Here d is the depth from the gate to the 2DEG, ϵ is the dielectric constant, and L is the length of the device between Ohmic contacts. Taking parameters from (11) and assuming a single-sided hBN substrate with dielectric constant $\epsilon_{\text{hBN}} = 4.4$ [8] such that $\epsilon = 2.7$ and assuming $d = 50$ nm, the gate voltage may be estimated as $\varphi_g \approx 3.4$ V. For channel length $L = 100$ μm the voltage drop along the device is $\varphi \approx 0.6$ mV. Hence $\delta n/n \sim \varphi/\varphi_g \sim 2 \times 10^{-4}$. The incompressible approximation is valid.

III. BOUNDARY LAYER FOR A STRAIGHT SEMI-INFINITE CHANNEL WITH NO-SLIP BOUNDARY CONDITION

This section has two goals: (i) to estimate the width of the boundary layer, and (ii) to point out some qualitative effects related to the boundary layer. In this section, we disregard the subleading gradient correction and use the standard Navier-Stokes equation (1).

A. Boundary-layer flow in the perturbative limit $\omega\tau \ll 1$

Consider a semi-infinite straight channel with a no-slip boundary at $y = 0$ and fluid flow in the region $y > 0$. In conjunction with the Stokes equation (1), the stream function must satisfy the no-penetration and no-slip boundary conditions,

$$v_y|_{y=0} = -\partial_x\psi|_{y=0} = 0, \;\; v_x|_{y=0} = \partial_y\psi|_{y=0} = 0. \tag{13}$$

The no-penetration condition ensures that no fluid can cross the boundary, whereas the no-slip condition ensures that the fluid has zero tangential velocity at the boundary surface. Furthermore, the stream function must decay to the bulk solution (5) far from the boundary. We look for a solution as an expansion in powers of $\omega\tau \ll 1$, i.e., $\psi = \sum_{n=0}^{\infty}(\omega\tau)^n\psi^{(n)}$. First we solve for the zero-order solution, corresponding to flow in the absence of a magnetic field. Solving the Stokes equation for $\omega\tau = 0$ using the boundary conditions leads to the Poiseuille solution

$$\psi^{(0)} = v_0(y + De^{-y/D}). \tag{14}$$

Next, introducing the magnetic field as a perturbation, we derive the first-order correction in the solution, $\psi = \psi^{(0)} + \omega\tau\psi^{(1)}$,

$$\psi^{(1)} = v_0\cos(gx)\left(\frac{1}{g(1+g^2D^2)} + Ae^{-y/D} + C_1e^{-gy} + C_2e^{-\sqrt{g^2+\frac{1}{D^2}}y}\right), \tag{15}$$

where the coefficients A, C_1, and C_2 are defined as

$$A = \frac{1}{g(1-g^2D^2)},$$

$$C_1 = \frac{2(g^2D^2+1)^{-\frac{1}{2}} - 1}{g(1-g^2D^2)(gD - \sqrt{g^2D^2+1})},$$

$$C_2 = \frac{1-gD}{g(1+gD)(1+g^2D^2)(gD-\sqrt{g^2D^2+1})}.$$

Note that in the case of $gD \to 1$, the coefficients $A, C_1 \to \infty$. However, it is easy to check that the divergences compensate each other such that the solution remains finite.

To maximize the viscous dissipation, we are interested in the case $gD > 1$. Since the slowest decaying boundary term in Eq. (15) decays as $e^{-y/D}$, the characteristic viscous length D sets the width of the boundary layer.

B. Exact numerical solution for the boundary-layer flow

While the perturbative solution for the boundary layer presented in the previous subsection is illuminating, for practical purposes we must find the solution at $\omega\tau > 1$. This can only be done numerically. To do so, we reduce the Stokes equation (1) to an infinite series of linear algebraic equations. We then numerically solve these equations by truncating them at a suitable order.

We consider a semi-infinite channel $y \geqslant 0$ and use length units where $D = \sqrt{\nu\tau} = 1$ and velocity units where $v_0 = 1$. As the magnetic field is periodic in the x direction, so is the stream function ψ, which can thus be presented as the following Fourier series:

$$\psi = y + e^{-y} + \frac{\omega\tau}{g(g^2+1)}\cos(gx) + \sum_{m=-\infty}^{\infty} e^{igmx}G_m(y). \tag{16}$$

Here m is an integer and $G_m(y)$ are unknown functions that must decay with increasing y as the solution tends to the bulk solution far from the boundary. Thus, using the perturbative solution as a starting point, we consider solutions of the form

$$G_m(y) = f_m e^{-y} + \sum_a A_{m,a}e^{-\lambda_a y}, \tag{17}$$

where f_m and $A_{m,a}$ are complex coefficients. The index $a = 1, 2, 3, \ldots$ enumerates "eigenvalues" λ_a, which can be real or complex. The real parts of λ_a are positive by design of Eq. (17). In practice, the upper limit of the index a, $a_{\max} = 2N_m + 1$, is fixed by truncation. Since the "Bernoulli term" is

neglected, the Stokes equation (1) is a linear equation. Let us consider the Poiseuille solution without a magnetic field,

$$\psi_0 = y + e^{-y}, \tag{18}$$

as a base solution. Now, in a magnetic field the stream function has a driven part correction, $\delta\psi_d$, driven by ψ_0, and a free part correction, $\delta\psi_f$,

$$\begin{aligned}\psi &= \psi_0 + \delta\psi_d + \delta\psi_f,\\ \delta\psi_d &= \frac{\omega\tau}{g(g^2+1)}\cos(gx) + \sum_{m=-\infty}^{\infty} e^{igmx} f_m e^{-y},\\ \delta\psi_f &= \sum_{m=-\infty}^{\infty} e^{igmx} \sum_a A_{m,a} e^{-\lambda_a y}.\end{aligned} \tag{19}$$

The first term in $\delta\psi_d$ is driven by the first term in Eq. (18) and the second term in $\delta\psi_d$ is driven by the second term in Eq. (18). Hence, the function $G_m(y)$ in Eq. (17) is a combination of a driven part and a free part. For a linear differential equation, the driven part is fully determined by the equation, but the coefficients in the free part are determined by the boundary conditions.

It is convenient to define the following differential operators:

$$\begin{aligned}\hat{D} &\equiv -\nabla^2 + \nabla^4,\\ \hat{d} &\equiv \omega\tau g\cos(gx)\partial_y.\end{aligned} \tag{20}$$

Using these notations, the Stokes equation can be rewritten as

$$\begin{aligned}(\hat{D} - \hat{d})\delta\psi_d &= \hat{d}\psi_0,\\ (\hat{D} - \hat{d})\delta\psi_f &= 0.\end{aligned} \tag{21}$$

Using the representation (19), the driven equation is transformed to an infinite set of linear algebraic equations for the coefficients f_m,

$$\begin{aligned}&(g^2m^2)(g^2m^2-1)f_m + \frac{\omega\tau g}{2}(f_{m+1} + f_{m-1})\\ &\quad = -\frac{\omega\tau g}{2}(\delta_{m,1} + \delta_{m,-1}).\end{aligned} \tag{22}$$

The coefficients in this equation are real and even in m. Therefore, the coefficients f_m are also real and even in m. For this reason, only equations for non-negative m are independent. A numerical solution of Eq. (22) is straightforward, with truncation beyond $m > N_m$, resulting in $N_m + 1$ independent equations. The second equation in Eqs. (21), i.e., the free equation, is transformed to an infinite set of linear algebraic equations for the coefficients A_m,

$$\begin{aligned}&\left(g^2m^2 - \lambda_a^2\right)\left(1 + g^2m^2 - \lambda_a^2\right)A_{m,a}\\ &\quad + \frac{\omega\tau g}{2}\lambda_a(A_{m+1,a} + A_{m-1,a}) = 0,\end{aligned} \tag{23}$$

noting that λ_a is independent of m. Again, only equations with non-negative m are independent, and we truncate m such that $m \leqslant N_m$. Hence the number of independent equations is again $N_m + 1$. The right-hand side of Eq. (23) is zero, so for a nontrivial solution the determinant of the matrix must be equal to zero. Hence, this is an eigenvalue problem but it is not a standard linear eigenvalue problem. To solve the eigenvalue problem, we calculate the determinant as a polynomial in λ and numerically determine the roots of the polynomial. The polynomial order is $4(N_m + 1)$. After we discard roots with a nonpositive real part, we are left with $2N_m + 1$ roots. Interestingly, at a sufficiently large $\omega\tau$ there are complex roots. The coefficients in the polynomial are real, so complex roots always come in complex conjugate pairs. We enumerate $2N_m + 1$ roots by the index a. For any found λ_a we solve Eqs. (23) and hence find the coefficients $A_{m,a}$, numerically determined to arbitrary normalization. We now write $A_{m,a} = \alpha_a A^{(n)}_{m,a}$, where $A^{(n)}_{m,a}$ is normalized such that $\sum_m |A^{(n)}_{m,a}|^2 = 1$, and α_a is an arbitrary coefficient.

The boundary conditions (13) provide a set of equations to determine the $2N_m + 1$ coefficients α_a,

$$\begin{aligned}&0 = v_y|_{y=0} \Longrightarrow\\ &m\left(f_m + \sum_a \alpha_a A^{(n)}_{m,a}\right) + \frac{\omega\tau}{2g(1+g^2)}(\delta_{m,1} - \delta_{m,-1}) = 0,\\ &0 = v_x|_{y=0} \Longrightarrow\\ &f_m + \sum_a \lambda_a\alpha_a A^{(n)}_{m,a} = 0.\end{aligned} \tag{24}$$

The first of these equations is nontrivial at $m = 1, 2, \ldots, N_m$ and the second equation is nontrivial at $m = 0, 1, \ldots, N_m$, so altogether we have $2N_m + 1$ equations to determine $2N_m + 1$ unknown coefficients α_a. Thus the boundary-layer problem is solved.

The boundary-layer solution is extended to finite width channels in Appendix A. After the method is developed, it is instructive to present plots for specific cases. For the numerical solution we set $gD = 0.88$, which corresponds to the device described at the end of Sec. II. We truncate beyond $N_m = 5$, which provides more than sufficient accuracy for the values of $\omega\tau$ we present. Plots of the streamlines obtained for $\omega\tau = 0.2$, 1.2, and 2.4 are presented in Fig. 1. These values of $\omega\tau$ were selected as $\omega\tau = 0.2$ has only real eigenvalues λ_a and corresponds to the perturbative regime, $\omega\tau = 1.2$ has a complex conjugate pair of eigenvalues λ_a and corresponds to the device described in Eq. (11), and $\omega\tau = 2.4$ has two complex conjugate pairs of eigenvalues λ_a. As the magnetic field increases ($\omega\tau$ increases), both the magnitude of the boundary effects and the width of the boundary layer increase. For the most interesting case, $\omega\tau \approx 1$, the effective width of the boundary layer is approximately D. Therefore, for the set of parameters (11) a channel of width = 10–20 μm is sufficiently wide to neglect boundary-layer effects.

The boundary-layer solution considered in this section is valid for the no-slip boundary condition. However, the method can be easily extended to the case of an arbitrary slip length; see Appendix B for details.

IV. NUMERICAL ESTIMATES, ANTI-POISEUILLE FLOW

Following the numerical calculation of the stream function, we may calculate the viscous dissipation rate and the Ohmic dissipation rate given by Eqs. (7). The most important parameter is the ratio $\dot{E}_\nu/\dot{E}_\Omega$, which is dependent on the device considered, so to provide calculated values we take the device with parameters presented in Eq. (11). This corresponds to

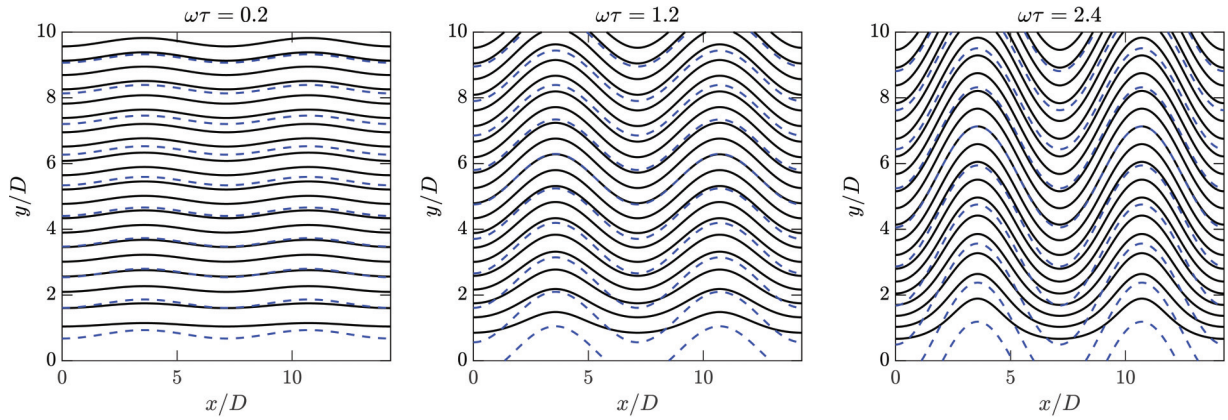

FIG. 1. Streamlines in a semi-infinite channel with a no-slip boundary at $y = 0$. The parameters are chosen as $gD = 0.88$, $\omega\tau = 0.2, 1.2, 2.4$. Solid lines correspond to the numerically exact solution described in Sec. III B, and dashed lines correspond to the solution given by Eq. (5) in the infinite device.

$D = 0.34$ μm. We also take the lattice spacing $a = 2.5$ μm as discussed in the end of Sec. II, resulting in $gD = 0.88$. The dissipation rates are plotted in Fig. 2 versus the channel width W for two values of the magnetic field amplitude—$B_0 = 75$ and 150 mT—corresponding to $\omega\tau = 1.2$ and 2.4, respectively. Solid lines correspond to solutions of the NS equation (1). The dashed line corresponds to total dissipation in the bulk from solution of the NS+ equation (3) where the gradient correction is significant, $C^2 = 1 \to C^2 = (1 - 0.19)^2 = 1 - 0.34$. In these plots we assume that the viscosity is independent of the magnetic field, $\nu(B) = \nu(0)$. Asymptotic values of the ratio $\dot{E}_\nu/\dot{E}_\Omega$ at $W \to \infty$ are 0.16 ($B_0 = 75$ mT) and 0.48 ($B_0 = 150$ mT). Note that as the magnetic field increases, the difference between the asymptotic value of the total dissipation from the NS equation and the total bulk dissipation from the NS$^+$ equation increases.

Now let us calculate the value of the correction of the first kind, as is discussed in the paragraph before Eq. (3). The viscosity is often reported to depend on magnetic field, with a possible dependence [10]

$$\nu \to \frac{\nu}{1 + (B/B^*)^2} \approx \nu[1 - (B/B^*)^2], \qquad B^* = \frac{p_F}{2|e|l_{\rm ee}}. \tag{25}$$

The term $\nu(B/B^*)^2\nabla^2\mathbf{v}$ added to the Navier-Stokes equation (1) leads to the correction of the first kind. We call it "the amplitude correction." It is easy to calculate the correction by perturbation theory. In perturbation theory it does not influence the Ohmic dissipation, but in calculating the viscous dissipation in Eq. (6), as $B = B(x)$ gives $\nu = \nu(x)$, one has to move ν in the integrand and perform integration over position. This gives the following correction to the viscous dissipation:

$$\frac{\delta\dot{E}_\nu}{\dot{E}_\nu} = -3(\omega\tau)^2\left(\frac{l_{\rm ee}}{l_{\rm mfp}}\right)^2. \tag{26}$$

The correction is -7% for $\omega\tau = 1.2$ and -28% for $\omega\tau = 2.4$. Note that by performing experiments for different values of a and different values of the magnetic field amplitude, it is possible to disentangle and to measure independently the viscosity, the gradient correction (Hall viscosity), and the amplitude correction (26).

Interestingly, the fluid flow in the boundary layer shows a sort of anti-Poiseuille behavior. To illustrate this, we plot in Fig. 3 the longitudinal velocity v_x versus y (i.e., across the channel). The velocity v_x is a function of both x and y, and here we present plots at $x = 0$. At a sufficiently large magnetic field, $\omega\tau \gtrsim 1.2$, there is a clear anti-Poiseuille profile near the left boundary of the channel. In this regime, the peak velocity is not v_0 in the bulk, but instead the longitudinal velocity has a maximum in the boundary layer before decaying towards v_0 in the bulk. There is a conventional Poiseuille behavior at the right boundary of the channel, although at high magnetic field a small amount of counterflow develops due to the development of vortices in the boundary layer. If we shift $x = 0 \to x = a/2$ the plots are effectively reflected about the center of the channel: the anti-Poiseuille profile is located at the right boundary and the Poiseuille profile is at the left boundary. Mathematically, the anti-Poiseuille profile is related to the complex eigenvalues λ_a. This behavior is qualitatively similar to the anti-Poiseuille flow predicted for narrow graphene channels near charge neutrality in the presence of a uniform magnetic field perpendicular to the plane [50–52]. Near charge neutrality this effect is largely attributed to electron-hole recombination. In our case, the physical origin of the anti-Poiseuille profile is different as we do not have any holes. While we consider no-slip boundaries, a similar anti-Poiseuille profile exists also for boundary conditions with a finite slip length; see Appendix B.

V. FINITE-ELEMENT SIMULATIONS

To complement our numerical results and to extend them towards finite systems, we also performed numerical simulations using the finite-element method (FEM). The first step is to bring Eq. (1) to the form of a weak differential equation by multiplying each of the equations with a test function and integrating over all space. We again neglect the Bernoulli term because we assume small flow velocity and that the fluid is incompressible. For the finite-element analysis, we use the space of Lagrange polynomials of second order as the

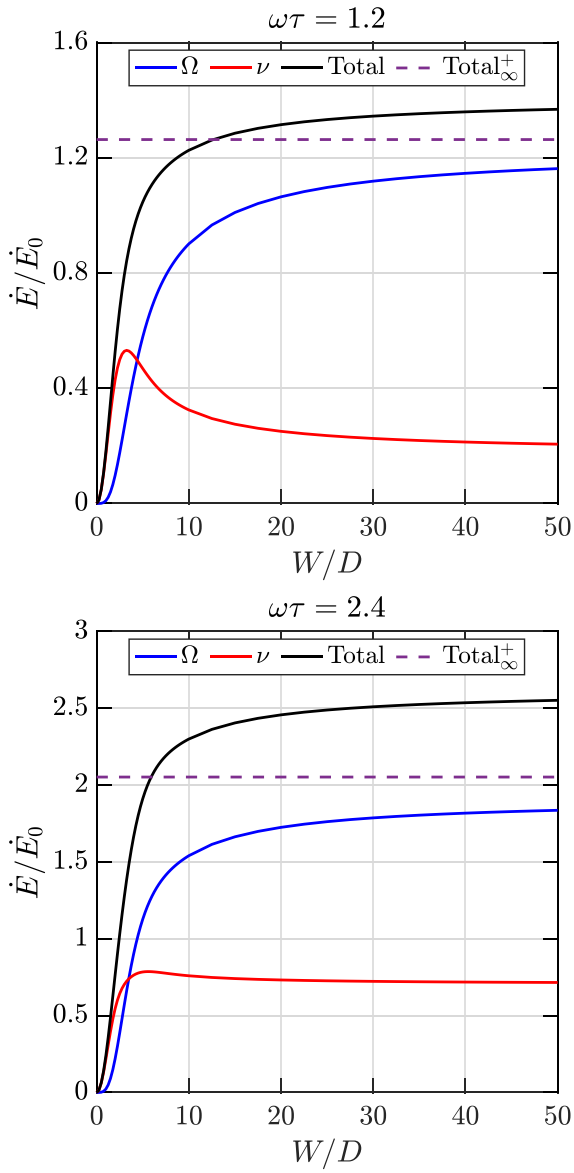

FIG. 2. Ohmic, viscous, and total dissipation from solution of the NS equation (1) as a function of channel width and total dissipation in the bulk from solution of the NS^+ equation (3). The dissipation is normalized to the $\dot{E}_0$, which is due to Drude resistance only, i.e., which is expected in the absence of B-field and hydrodynamics ($\dot{E}_0/LW = nm^*v_0^2/\tau$). The value $\omega\tau = 1.2$ corresponds to $B_0 = 75$ mT and $\omega\tau = 2.4$ corresponds to $B_0 = 150$ mT. In these plots we assume that the viscosity is independent of the magnetic field, $\nu(B) = \nu(0)$. The plots correspond to the parameter set (11), where $gD = 0.88$.

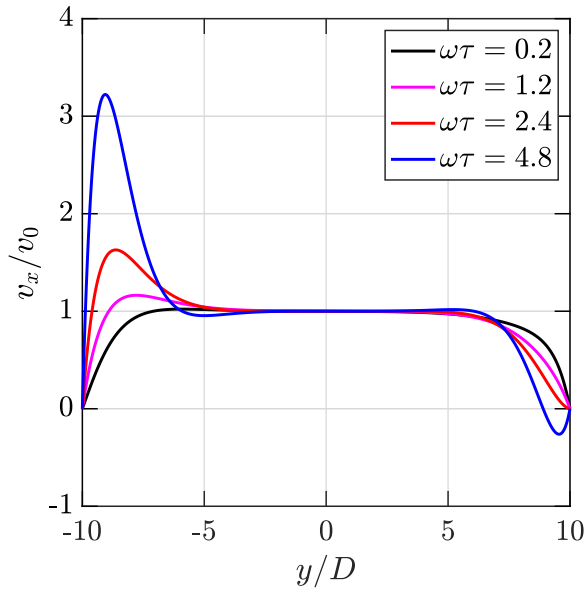

FIG. 3. Longitudinal velocity profile at $x/D = 0$ with $gD = 0.88$ for various values of $\omega\tau$. At large magnetic fields anti-Poiseuille flow is observed and a small counterflow is observed at the opposite boundary due to the formation of a viscous vortex.

function space for the velocity field and the space of Lagrange polynomials of first order as the function space for the potential. Together these form a Taylor-Hood element appropriate for the numerical solution of Navier-Stokes equations. We have numerically implemented the problem using the *FEniCS* package [57].

Using FEM, we consider a finite system with a rectangular geometry with width W in the y direction and length L in the x direction. To simulate a finite array of micromagnets, we consider a flow driven by an applied electric potential difference, so we assume Dirichlet boundary conditions for the voltage $\varphi(x = -L/2, y) = \varphi_L$ and $\varphi(x = L/2, y) = \varphi_R$ at the inlet and outlet. In addition to this, we assume that $v_y(x = \pm L/2, y) = 0$ at both the inlet and outlet. Finally, we impose no-slip boundary conditions at the walls, i.e., $\mathbf{v}(x, y = \pm W/2) = 0$.

Figure 4 shows that the results of these simulations qualitatively reproduce all features found for the infinite system. At strong enough magnetic fields, an anti-Poiseuille flow emerges near the boundary. Moreover, at strong fields, a small counterflow becomes visible at the opposite boundary.

VI. MAGNETIC FIELD OF PERIODIC FERROMAGNETIC STRIPES

The setup considered in this paper is similar to the setup previously proposed for GaAs heterostructure in Ref. [53], but adapted to suit monolayer graphene with parameters described in Eq. (11). A superlattice of rectangular magnetic bars oriented perpendicular to the longitudinal axis of the device is placed above the 2DEG as seen in the left panel of Fig. 5. The thickness of each micromagnet is δz and the distance from the base of each micromagnet to the 2DEG is z, shown in the right panel of Fig. 5. The period of modulation is $a = 2.5$ μm, as found in Sec. II. The micromagnets are magnetized parallel to the longitudinal axis of the channel. The remaining free parameters $d, z, \delta z$ are tuned such that the z component of the magnetic field in the plane of the 2DEG is approximately $B_0 \sin(2\pi x/a)$ with $B_0 \approx 75$ mT. A stronger magnetic field may also be achieved.

Assuming the magnetization is uniform throughout the volume of each micromagnet, and each micromagnet's extent in the transverse (y) direction is wider than the width W of the

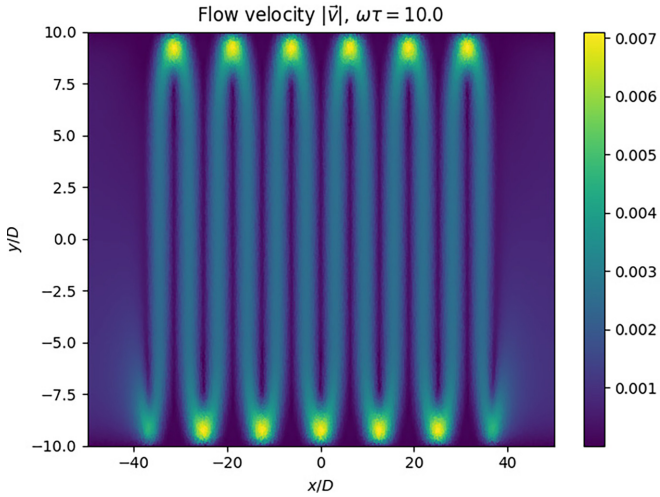

FIG. 4. FEM results for the absolute value $|\mathbf{v}|$ of the velocity in a finite channel of length $L = 100D$ for $gD = 0.5$. There is an equilibration region near the inlet and outlet where uniform flow transitions to periodic flow, with periodic flow established from $-40 < x/D < 40$. Note that this color plot should not be confused with lines of flow, which are shown in Fig. 1 The velocity is measured in units convenient for numerical solution, and the system contains six magnetic strips. The region of high velocity, anti-Poiseuille flow, is shifted by half a period at opposite boundaries.

sample, we calculate the z component of the magnetic field in the plane of the 2DEG as a function of longitudinal coordinate x from the Biot-Savart law as

$$\left.\frac{B_z(x)}{B_m}\right|_{\text{2DEG}} = -\sum_{n>1} \frac{\sin(gnd/2)}{\pi n} \sin(gnx) Z_n,$$

$$Z_n(z, \delta z) = e^{-gnz}(1 - e^{-gn\delta z}), \tag{27}$$

where B_m is the saturation magnetic field, and x is measured from the center of one of the micromagnets. At the edge of the micromagnet centered on $x = d/2$, the harmonics of the field in the 2DEG plane is $\propto \sin^2(gnd/2)$, so evidently $d = a/2 = \pi/g$ maximizes the first harmonic and suppresses the second harmonic. We calculate B numerically from Eq. (27) and confirm that $d = a/2 = 1.25$ μm is optimal.

To achieve a field with magnitude $B_0 = 75$ mT, we consider a NiFe alloy that has a saturation magnetic field

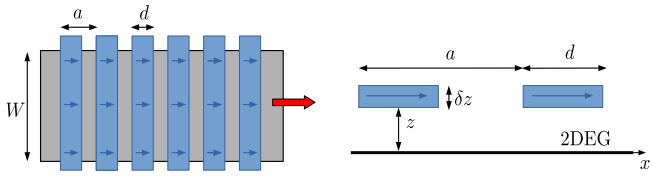

FIG. 5. Left: top view of a periodic array of magnetic bars perpendicular to the flow direction shown by the red arrow. The micromagnets are magnetized parallel to the longitudinal axis of the channel. The direction of the magnetization is shown by the blue arrows. The period of the superlattice is a and the width of each micromagnet is d. Right: Side view of the device. The vertical distance from the micromagnets to the 2DEG is z and the thickness of each micromagnet is δz. First presented in Ref. [53].

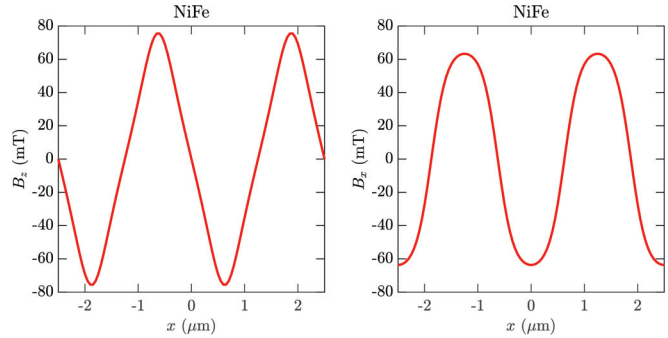

FIG. 6. Magnetic field in the 2DEG plane for NiFe bars. Left panel: B_z vs x. Right panel: B_x vs x. The parameters are $\delta z = 0.20$ μm, $z = 0.40$ μm.

1500 mT [58]. Through concurrently tuning δz and z, we find that we may generate the desired magnetic field profile with $\delta z = 0.20$ μm and $z = 0.40$ μm. Plots of B_z versus x and B_x versus x are presented in Fig. 6. The x component of the magnetic field is not relevant, but we present it for completeness. The x dependence of B_z is not quite sinusoidal, however this is not a big issue as by using the finite-element method, one can also solve the Navier-Stokes equation for this magnetic field profile. It should be noted that any magnetic disorder due to a slight misalignment of the micromagnets with respect to the channel or inconsistencies in the spacing or width of the micromagnets results in high wave-number contributions to the magnetic field, with these contributions exponentially suppressed due to the distance z between the micromagnets and the 2DEG, as seen in Eq. (27).

VII. CONCLUSIONS

We develop a theory for the no-slip boundary layer in the magnetohydrodynamic flow of an electron fluid in a straight channel. The fluid flow is modified by an array of micromagnets on the top of two-dimensional electron gas. The micromagnets create a wiggling flow of the fluid, which dramatically enhances hydrodynamic effects in the fluid. To be specific, the analysis was performed for no-slip boundary conditions, but the method can be extended to boundary conditions with arbitrary slip length. We demonstrate that the fluid velocity profile in the boundary layer manifests an anti-Poiseuille behavior. In addition, we show that the micromagnet array creates a longitudinal voltage modulation in the sample. From the experimental point of view, we propose a method for a boundary-independent measurement of the viscosity of different electron fluids. The results are applicable to graphene away from the charge-neutrality point and also to semiconductors.

ACKNOWLEDGMENTS

We acknowledge important discussions with A. Hamilton, Y. A. Alava, O. Klochan, D. Wang, and Z. Krix. This work was supported by the Australian Research Council Centre of Excellence in Future Low-Energy Electronics Technologies (CE170100039).

APPENDIX A: THE METHOD FOR AN EXACT SOLUTION FOR A FINITE WIDTH CHANNEL

Here we expand the method of Sec. III to a finite channel with no-slip boundaries at $y = \pm W/2$. Here we use units $D = v_0 = 1$. As before we split the stream function into the zero field term, which corresponds to Poiseuille flow, ψ_0, the driven magnetic field correction term, $\delta\psi_f$, and the free magnetic field correction term, $\delta\psi_d$,

$$\begin{aligned}\psi &= \psi_0 + \delta\psi_d + \delta\psi_f,\\ \psi_0 &= y - \frac{\sinh y}{\cosh W/2}\\ \delta\psi_d &= \frac{\omega\tau}{g(g^2+1)}\cos(gx) + \sum_{m=-\infty}^{\infty} e^{igmx}(f_m e^{-y} + h_m e^{y}),\\ \delta\psi_f &= \sum_{m=-\infty}^{\infty} e^{igmx}\sum_a (A_{m,a}e^{-\lambda_a y} + C_{m,a}e^{\lambda_a y}).\end{aligned} \tag{A1}$$

Note that we absorb the constant exponential terms into the unknown coefficients. The stream function solves the Stokes' equation as in Eq. (21). From the driven equation, we obtain a set of equations for coefficients f_m and h_m.

$$\begin{aligned}&(g^2m^2)(g^2m^2-1)f_m + \frac{\omega\tau g}{2}(f_{m+1}+f_{m-1})\\ &\quad = -\frac{\omega\tau g}{4\cosh W/2}(\delta_{m,1}+\delta_{m,-1}),\\ &(g^2m^2)(g^2m^2-1)h_m - \frac{\omega\tau g}{2}(h_{m+1}+h_{m-1})\\ &\quad = -\frac{\omega\tau g}{4\cosh W/2}(\delta_{m,1}+\delta_{m,-1}).\end{aligned} \tag{A2}$$

As the coefficients are real and even in m, f_m and h_m are also real and even in m. The free equation gives eigenequations for eigenvalues λ_a and eigenvectors $A_{m,a}$ and $C_{m,a}$,

$$\begin{aligned}&\big(g^2m^2-\lambda_a^2\big)\big(1+g^2m^2-\lambda_a^2\big)\big)A_{m,a}\\ &\quad +\frac{\omega\tau g}{2}\lambda_a(A_{m+1}+A_{m-1}) = 0,\\ &\big(g^2m^2-\lambda_a^2\big)\big(1+g^2m^2-\lambda_a^2\big)\big)C_{m,a}\\ &\quad -\frac{\omega\tau g}{2}\lambda_a(C_{m+1}+C_{m-1}) = 0.\end{aligned} \tag{A3}$$

Note that the determinant of the A-equation is identical to that of the C-equation. Hence, there is only one set of eigenvalues λ_a which we find following the method described in the main text. The eigenvectors $A_{m,a}$ and $C_{m,a}$ are different, and we find them solving Eqs. (A3). The eigenvectors are determined up to some arbitrary normalization. Similarly to the approach in Sec. III, we define coefficients α_a and γ_a and write $A_{m,a} = \alpha_a A^{(n)}_{m,a}$ and $C_{m,a} = \gamma_a C^{(n)}_{m,a}$, where $\sum_m |A^{(n)}_{m,a}|^2 = 1$ and $\sum_m |C^{(n)}_{m,a}|^2 = 1$, and α_a and γ_a are arbitrary coefficients. These coefficients are determined by considering the boundary conditions at $y = \pm\frac{W}{2}$,

$$\begin{aligned}&0 = v_y|_{y=\pm W/2} \to\\ &m\Bigg[f_m e^{\mp W/2} + h_m e^{\pm W/2} + \sum_a \big(\alpha_a A^{(n)}_{m,a} e^{\mp\lambda_a W/2}\\ &\quad + \gamma_a C^{(n)}_{m,a} e^{\pm\lambda_a W/2}\big)\Bigg] + \frac{\omega\tau}{2g(1+g^2)}(\delta_{m,1}-\delta_{m,-1}) = 0,\end{aligned}$$

$$\begin{aligned}&0 = v_x|_{y=\pm W/2} \to\\ &\sum_a \lambda_a\big(\alpha_a A^{(n)}_{m,a} e^{\mp\lambda_a W/2} - \gamma_a C^{(n)}_{m,a} e^{\pm\lambda_a W/2}\big)\\ &+ f_m e^{\mp W/2} - h_m e^{\pm W/2} = 0.\end{aligned} \tag{A4}$$

Upon solving Eq. (A4) and obtaining α_a and γ_a, the stream function is entirely characterized, and velocity and dissipation profiles may be calculated.

APPENDIX B: SOLUTION FOR BOUNDARIES WITH FINITE SLIP LENGTH

We now expand upon the solution for the finite channel to account for some finite slip length, β, defined in the finite slip boundary condition [59]. Note the change in sign of β at the positive and negative y boundaries,

$$v_x|_{y=\pm W/2} = \mp\beta\partial_y v_x|_{y=\pm W/2}. \tag{B1}$$

The no-penetration boundary condition remains unchanged. We must first account for the finite-slip boundary in our definition of ψ_0, which we do by considering flow in the absence of a periodic magnetic field. This is simply the following:

$$\psi_0 = y + \frac{e^{-y} - e^{y}}{e^{w/2}(1+\beta) + e^{-w/2}(1-\beta)}. \tag{B2}$$

While the equations for the free solution, Eq. (A3), remain unchanged, the equations for the driven solution, Eq. (A2), are

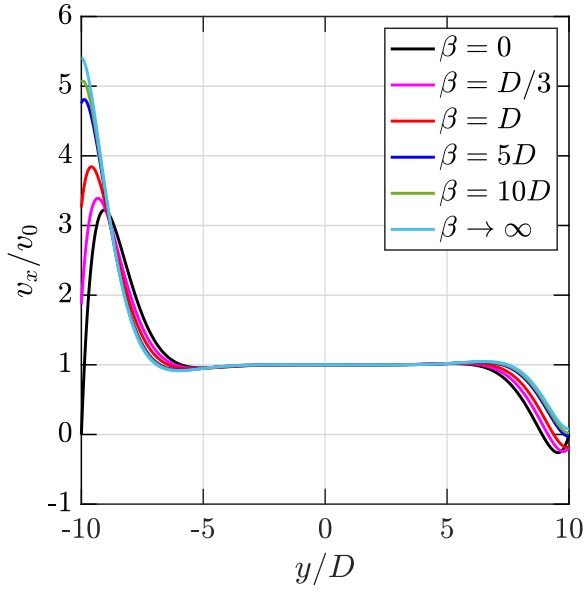

FIG. 7. Longitudinal velocity profile at $x/D = 0$ with $gD = 0.88$ and $\omega\tau = 4.8$ for a range of slip length β. Clearly the finite-slip cases interpolate between the no-slip and perfect-slip cases. As β increases, the strength of the anti-Poiseuille flow peak increases until it saturates at the perfect-slip level, while counterflow at the other boundary quickly disappears with finite β.

modified by the redefinition of ψ_0,

$$
\begin{aligned}
&(g^2m^2)(g^2m^2-1)f_m + \frac{\omega\tau g}{2}(f_{m+1}+f_{m-1}) \\
&\quad = -\frac{\omega\tau g}{2[e^{w/2}(1+\beta)+e^{-w/2}(1-\beta)]}(\delta_{m,1}+\delta_{m,-1}), \\
&(g^2m^2)(g^2m^2-1)h_m - \frac{\omega\tau g}{2}(h_{m+1}+h_{m-1}) \\
&\quad = -\frac{\omega\tau g}{2[e^{w/2}(1+\beta)+e^{-w/2}(1-\beta)]}(\delta_{m,1}+\delta_{m,-1}).
\end{aligned}
\tag{B3}
$$

Now, while the no-penetration boundary condition remains unchanged, we must solve the finite-slip boundary condition for $\delta\psi_d + \delta\psi_f$. The no-penetration and finite slip boundary conditions applied to the finite channel system are as follows:

$$
\begin{aligned}
&0 = v_y|_{y=\pm W/2} \rightarrow \\
&\quad m\Bigg[f_m e^{\mp W/2} + h_m e^{\pm W/2} + \sum_a \left(\alpha_a A^{(n)}_{m,a} e^{\mp\lambda_a W/2}\right. \\
&\qquad \left.+\gamma_a C^{(n)}_{m,a} e^{\pm\lambda_a W/2}\right)\Bigg] + \frac{\omega\tau}{2g(1+g^2)}(\delta_{m,1}-\delta_{m,-1}) = 0,
\end{aligned}
$$

$$
\begin{aligned}
&v_x|_{y=\pm W/2} = \mp\beta\partial_y v_x|_{y=\pm W/2} \rightarrow \\
&\sum_a \lambda_a\left(\alpha_a A^{(n)}_{m,a} e^{\mp\lambda_a W/2} - \gamma_a C^{(n)}_{m,a} e^{\pm\lambda_a W/2}\right) \\
&\quad + f_m e^{\mp W/2} - h_m e^{\pm W/2} = \mp\beta\Bigg(f_m e^{\mp W/2} + h_m e^{\pm W/2} \\
&\quad + \sum_a \lambda_a^2\left(\alpha_a A^{(n)}_{m,a} e^{\mp\lambda_a W/2} + \gamma_a C^{(n)}_{m,a} e^{\pm\lambda_a W/2}\right)\Bigg).
\end{aligned}
\tag{B4}
$$

It is instructive to compare the no-slip, finite-slip, and perfect-slip cases. For monolayer graphene, the slip length is dependent on temperature and has been found, as a fitting parameter, to be on the order of 0.5–0.1 μm for $T = 300$ K [22] and $T = 75$ K [23]. For the parameters we consider in this manuscript, an appropriate choice is $\beta = D/3$. In Fig. 7 we present v_x profiles for $\omega\tau = 4.8$ for the different boundary conditions, with this $\omega\tau$ chosen to highlight anomalous flow behavior. As the β is increased, the flow transitions from the no-slip case to the perfect-slip case, with the anti-Poiseuille flow peak increasing with increasing β and counterflow at the opposite boundary quickly vanishing with small finite β. At a realistic slip length $\beta = D/3$, one would expect strong periodic anti-Poiseuille flow as well as small finite counterflow.

[1] R. N. Gurzhi, Hydrodynamic effects in solids at low temperature, Sov. Phys. Usp. **11**, 255 (1968).

[2] M. Polini and A. K. Geim, Viscous electron fluids, Phys. Today **73**, 28 (2020).

[3] B. N. Narozhny, Hydrodynamic approach to two-dimensional electron systems, Riv. Nuovo Cimento **45**, 661 (2022).

[4] R. N. Gurzhi, Minimum of Resistance in Impurity-free Conductors, Sov. Phys. JETP **17**, 521 (1963).

[5] M. J. M. de Jong and L. W. Molenkamp, Hydrodynamic electron flow in high-mobility wires, Phys. Rev. B **51**, 13389 (1995).

[6] A. Lucas and K. C. Fong, Hydrodynamics of electrons in graphene, J. Phys.: Condens. Matter **30**, 053001 (2018).

[7] R. N. Gurzhi, A. N. Kalinenko, and A. I. Kopeliovich, Electron-electron collisions and a new hydrodynamic effect in two-dimensional electron gas, Phys. Rev. Lett. **74**, 3872 (1995).

[8] D. A. Bandurin, I. Torre, R. K. Kumar, M. Ben Shalom, A. Tomadin, A. Principi, G. H. Auton, E. Khestanova, K. S. Novoselov, I. V. Grigorieva, L. A. Ponomarenko, A. K. Geim, and M. Polini, Negative local resistance caused by viscous electron backflow in graphene, Science **351**, 1055 (2016).

[9] P. J. W. Moll, P. Kushwaha, N. Nandi, B. Schmidt, and A. P. Mackenzie, Evidence for hydrodynamic electron flow in $PdCoO_2$, Science **351**, 1061 (2016).

[10] P. S. Alekseev, Negative magnetoresistance in viscous flow of two-dimensional electrons, Phys. Rev. Lett. **117**, 166601 (2016).

[11] R. Krishna Kumar, D. A. Bandurin, F. M. D. Pellegrino, Y. Cao, A. Principi, H. Guo, G. H. Auton, M. Ben Shalom, L. A. Ponomarenko, G. Falkovich, K. Watanabe, T. Taniguchi, I. V. Grigorieva, L. S. Levitov, M. Polini, and A. K. Geim, Superballistic flow of viscous electron fluid through graphene constrictions, Nat. Phys. **13**, 1182 (2017).

[12] D. A. Bandurin, A. V. Shytov, L. S. Levitov, R. K. Kumar, A. I. Berdyugin, M. Ben Shalom, I. V. Grigorieva, A. K. Geim, and G. Falkovich, Fluidity onset in graphene, Nat. Commun. **9**, 4533 (2018).

[13] A. C. Keser, D. Q. Wang, O. Klochan, D. Y. H. Ho, O. A. Tkachenko, V. A. Tkachenko, D. Culcer, S. Adam, I. Farrer, D. A. Ritchie, O. P. Sushkov, and A. R. Hamilton, Geometric control of universal hydrodynamic flow in a two-dimensional electron fluid, Phys. Rev. X **11**, 031030 (2021).

[14] G. M. Gusev, A. D. Levin, E. V. Levinson, and A. K. Bakarov, Viscous transport and Hall viscosity in a two-dimensional electron system, Phys. Rev. B **98**, 161303(R) (2018).

[15] L. V. Ginzburg, C. Gold, M. P. Röösli, C. Reichl, M. Berl, W. Wegscheider, T. Ihn, and K. Ensslin, Superballistic electron flow through a point contact in a Ga[Al]As heterostructure, Phys. Rev. Res. **3**, 023033 (2021).

[16] I. V. Gornyi and D. G. Polyakov, Two-dimensional electron hydrodynamics in a random array of impenetrable obstacles: Magnetoresistivity, Hall viscosity, and the Landauer dipole, Phys. Rev. B **108**, 165429 (2023).

[17] G. M. Gusev, A. D. Levin, E. V. Levinson, and A. K. Bakarov, Viscous electron flow in mesoscopic two-dimensional electron gas, AIP Adv. **8**, 025318 (2018).

[18] Q. Shi, P. D. Martin, Q. A. Ebner, M. A. Zudov, L. N. Pfeiffer, and K. W. West, Colossal negative magnetoresistance in a two-dimensional electron gas, Phys. Rev. B **89**, 201301(R) (2014).

[19] R. G. Mani, A. Kriisa, and W. Wegscheider, Size-dependent giant-magnetoresistance in millimeter scale GaAs/AlGaAs 2D electron devices, Sci. Rep. **3**, 2747 (2013).

[20] X. Wang, P. Jia, R.-R. Du, L. N. Pfeiffer, K. W. Baldwin, and K. W. West, Hydrodynamic charge transport in gaas/algaas ultrahigh-mobility two-dimensional electron gas, Phys. Rev. B **106**, L241302 (2022).

[21] A. D. Levin, G. M. Gusev, A. S. Yaroshevich, Z. D. Kvon, and A. K. Bakarov, Geometric engineering of viscous magnetotransport in a two-dimensional electron system, Phys. Rev. B **108**, 115310 (2023).

[22] J. A. Sulpizio, L. Ella, A. Rozen, J. Birkbeck, D. J. Perello, D. Dutta, M. Ben-Shalom, T. Taniguchi, K. Watanabe, T. Holder, R. Queiroz, A. Principi, A. Stern, T. Scaffidi, A. K. Geim, and S. Ilani, Visualizing Poiseuille flow of hydrodynamic electrons, Nature (London) **576**, 75 (2019).

[23] M. J. H. Ku, T. X. Zhou, Q. Li, Y. J. Shin, J. K. Shi, C. Burch, L. E. Anderson, A. T. Pierce, Y. Xie, A. Hamo, U. Vool, H. Zhang, F. Casola, T. Taniguchi, K. Watanabe, M. M. Fogler, P. Kim, A. Yacoby, and R. L. Walsworth, Imaging viscous flow of the Dirac fluid in graphene, Nature (London) **583**, 537 (2020).

[24] L. Ella, A. Rozen, J. Birkbeck, M. Ben-Shalom, D. Perello, J. Zultak, T. Taniguchi, K. Watanabe, A. K. Geim, S. Ilani, and J. A. Sulpizio, Simultaneous voltage and current density imaging of flowing electrons in two dimensions, Nat. Nanotechnol. **14**, 480 (2019).

[25] A. I. Berdyugin, S. G. Xu, F. M. D. Pellegrino, R. Krishna Kumar, A. Principi, I. Torre, M. Ben Shalom, T. Taniguchi, K. Watanabe, I. V. Grigorieva, M. Polini, A. K. Geim, and D. A. Bandurin, Measuring Hall viscosity of graphene's electron fluid, Science **364**, 162 (2019).

[26] A. O. Govorov and J. J. Heremans, Hydrodynamic effects in interacting Fermi electron jets, Phys. Rev. Lett. **92**, 026803 (2004).

[27] I. I. Kaya, Nonequilibrium transport and the Bernoulli effect of electrons in a two-dimensinoal electron gas, Mod. Phys. Lett. B **27**, 1330001 (2013).

[28] B. A. Braem, F. M. D. Pellegrino, A. Principi, M. Röösli, C. Gold, S. Hennel, J. V. Koski, M. Berl, W. Dietsche, W. Wegscheider, M. Polini, T. Ihn, and K. Ensslin, Scanning gate microscopy in a viscous electron fluid, Phys. Rev. B **98**, 241304(R) (2018).

[29] S. Samaddar, J. Strasdas, K. Janßen, S. Just, T. Johnsen, Z. Wang, B. Uzlu, S. Li, D. Neumaier, M. Liebmann, and M. Morgenstern, Evidence for local spots of viscous electron flow in graphene at moderate mobility, Nano Lett. **21**, 9365 (2021).

[30] Y.-T. Tu and S. Das Sarma, Wiedemann-Franz law in graphene, Phys. Rev. B **107**, 085401 (2023).

[31] J. Crossno, J. K. Shi, K. Wang, X. Liu, A. Harzheim, A. Lucas, S. Sachdev, P. Kim, T. Taniguchi, K. Watanabe, T. A. Ohki, and K. C. Fong, Observation of the Dirac fluid and the breakdown of the Wiedemann-Franz law in graphene, Science **351**, 1058 (2016).

[32] J. Gooth, F. Menges, N. Kumar, V. Süss, C. Shekhar, Y. Sun, U. Drechsler, R. Zierold, C. Felser, and B. Gotsmann, Thermal and electrical signatures of a hydrodynamic electron fluid in tungsten diphosphide, Nat. Commun. **9**, 4093 (2018).

[33] A. Lucas and S. Das Sarma, Electronic hydrodynamics and the breakdown of the Wiedemann-Franz and Mott laws in interacting metals, Phys. Rev. B **97**, 245128 (2018).

[34] A. Jaoui, B. Fauqué, and K. Behnia, Thermal resistivity and hydrodynamics of the degenerate electron fluid in antimony, Nat. Commun. **12**, 195 (2021).

[35] S. Ahn and S. Das Sarma, Hydrodynamics, viscous electron fluid, and Wiedeman-Franz law in two-dimensional semiconductors, Phys. Rev. B **106**, L081303 (2022).

[36] Y. Dai, R. R. Du, L. N. Pfeiffer, and K. W. West, Observation of a cyclotron harmonic spike in microwave-induced resistances in ultraclean GaAs/AlGaAs quantum wells, Phys. Rev. Lett. **105**, 246802 (2010).

[37] A. T. Hatke, M. A. Zudov, L. N. Pfeiffer, and K. W. West, Giant microwave photoresistivity in high-mobility quantum Hall systems, Phys. Rev. B **83**, 121301(R) (2011).

[38] M. Białek, J. Łusakowski, M. Czapkiewicz, J. Wróbel, and V. Umansky, Photoresponse of a two-dimensional electron gas at the second harmonic of the cyclotron resonance, Phys. Rev. B **91**, 045437 (2015).

[39] P. S. Alekseev and A. P. Alekseeva, Transverse magnetosonic waves and viscoelastic resonance in a two-dimensional highly viscous electron fluid, Phys. Rev. Lett. **123**, 236801 (2019).

[40] P. Gallagher, C.-S. Yang, T. Lyu, F. Tian, R. Kou, H. Zhang, K. Watanabe, T. Taniguchi, and F. Wang, Quantum-critical conductivity of the Dirac fluid in graphene, Science **364**, 158 (2019).

[41] G. Varnavides, A. S. Jermyn, P. Anikeeva, C. Felser, and P. Narang, Electron hydrodynamics in anisotropic materials, Nat. Commun. **11**, 4710 (2020).

[42] J. M. Link, B. N. Narozhny, E. I. Kiselev, and J. Schmalian, Out-of-Bounds Hydrodynamics in anisotropic Dirac fluids, Phys. Rev. Lett. **120**, 196801 (2018).

[43] A. Stern, T. Scaffidi, O. Reuven, C. Kumar, J. Birkbeck, and S. Ilani, How electron hydrodynamics can eliminate the Landauer-Sharvin resistance, Phys. Rev. Lett. **129**, 157701 (2022).

[44] V. Galitski, M. Kargarian, and S. Syzranov, Dynamo effect and turbulence in hydrodynamic Weyl metals, Phys. Rev. Lett. **121**, 176603 (2018).

[45] G. Tatara, Hydrodynamic theory of vorticity-induced spin transport, Phys. Rev. B **104**, 184414 (2021).

[46] R. J. Doornenbal, M. Polini, and R. A. Duine, Spin–vorticity coupling in viscous electron fluids, J. Phys.: Mater. **2**, 015006 (2019).

[47] M. Matsuo, D. A. Bandurin, Y. Ohnuma, Y. Tsutsumi, and S. Maekawa, Spin hydrodynamic generation in graphene, arXiv:2005.01493.

[48] R. Takahashi, M. Matsuo, M. Ono, K. Harii, H. Chudo, S. Okayasu, J. Ieda, S. Takahashi, S. Maekawa, and E. Saitoh, Spin hydrodynamic generation, Nat. Phys. **12**, 52 (2016).

[49] R. Takahashi, H. Chudo, M. Matsuo, K. Harii, Y. Ohnuma, S. Maekawa, and E. Saitoh, Giant spin hydrodynamic generation in laminar flow, Nat. Commun. **11**, 3009 (2020).

[50] P. S. Alekseev, A. P. Dmitriev, I. V. Gornyi, V. Y. Kachorovskii, B. N. Narozhny, and M. Titov, Counterflows in viscous electron-hole fluid, Phys. Rev. B **98**, 125111 (2018).

[51] P. S. Alekseev, A. P. Dmitriev, I. V. Gornyi, V. Y. Kachorovskii, B. N. Narozhny, and M. Titov, Nonmonotonic magnetoresistance of a two-dimensional viscous electron-hole fluid in a confined geometry, Phys. Rev. B **97**, 085109 (2018).

[52] B. N. Narozhny, I. V. Gornyi, and M. Titov, Anti-Poiseuille flow in neutral graphene, Phys. Rev. B **104**, 075443 (2021).

[53] J. N. Engdahl, A. C. Keser, and O. P. Sushkov, Micromagnets dramatically enhance effects of viscous hydrodynamic flow in a two-dimensional electron fluid, Phys. Rev. Res. **4**, 043175 (2022).

[54] L. Landau and E. Lifshitz, *Fluid Mechanics* (Elsevier Science, Kidlington, Oxfordshire, UK, 2013), Vol. 6.

[55] A. C. Keser and O. Sushkov, Magnetic response of a two-dimensional viscous electron fluid, Turk. J. Phys. **47**, 28 (2023).

[56] T. Scaffidi, N. Nandi, B. Schmidt, A. P. Mackenzie, and J. E. Moore, Hydrodynamic electron flow and Hall viscosity, Phys. Rev. Lett. **118**, 226601 (2017).

[57] H. Lantangen and A. Logg, *Solving PDEs in Python* (Springer, Cham, Switzerland, 2017).

[58] Magnetic Materials, in *Handbook of Magnetic Measurements*, Series in Sensors (CRC, Boca Raton, FL, 2011), Vol. 20110781, pp. 117–158.

[59] E. I. Kiselev and J. Schmalian, Boundary conditions of viscous electron flow, Phys. Rev. B **99**, 035430 (2019).